

# DnSwin: Toward Real-World Denoising via Continuous Wavelet Sliding-Transformer

Hao Li<sup>a</sup>, Zhijing Yang<sup>a</sup>, Xiaobin Hong<sup>b,\*</sup>, Ziyang Zhao<sup>c</sup>, Junyang Chen<sup>a</sup>,  
Yukai Shi<sup>a</sup>, Jinshan Pan<sup>d</sup>

<sup>a</sup>*School of Information Engineering, Guangdong University of  
Technology, Guangzhou, 510006, China*

<sup>b</sup>*School of Mechanical Automotive Engineering, South China University of  
Technology, Guangzhou, 510641, China*

<sup>c</sup>*School of Computer Science and Engineering, Sun Yat-sen  
University, Guangzhou, China*

<sup>d</sup>*School of Computer Science and Engineering, Nanjing University of Science and  
Technology, Nanjing, China*

---

## Abstract

Real-world image denoising is a practical image restoration problem that aims to obtain clean images from in-the-wild noisy input. Recently, Vision Transformer (ViT) exhibits a strong ability to capture long-range dependencies and many researchers attempt to apply ViT to image denoising tasks. However, real-world image is an isolated frame that makes the ViT build the long-range dependencies on the internal patches, which divides images into patches and disarranges the noise pattern and gradient continuity. In this article, we propose to resolve this issue by using a continuous Wavelet Sliding-Transformer that builds frequency correspondence under real-world scenes, called DnSwin. Specifically, we first extract the bottom features from noisy input images by using a CNN encoder. The key to DnSwin is to separate high-frequency and low-frequency information from the features and build frequency dependencies. To this end, we propose Wavelet Sliding-Window Transformer that utilizes discrete wavelet transform, self-attention and inverse discrete wavelet transform to extract deep features. Finally, we reconstruct the deep features into denoised images using a CNN decoder. Both quantitative and qualitative evaluations on real-world denoising benchmarks demonstrate that the proposed DnSwin performs favorably against

---

\*Corresponding author

the state-of-the-art methods.

*Keywords:* real-world image denoising, vision transformer, frequency correspondence, wavelet sliding-window

---

## 1. Introduction

Image denoising is a fundamental topic in low-level vision fields, which is widely applied in image restoration [1], super-resolution [2], optical flow [3], *etc.* It also plays an important role in pre-processing step of high-level computer vision tasks, such as object detection and image segmentation [4, 5]. The purpose of image denoising is aiming at restoring the latent clean images  $x$  from its noisy observation  $y$ . Traditional image denoising can be formulated as follows:

$$y = x + n. \tag{1}$$

where  $n$  is the additive noise that is generally modeled as a zero-mean white Gaussian noise with a standard deviation  $\sigma$ . To address the image degradation problems, lots of traditional image recovery models and learning-based methods have been developed in the past decades.

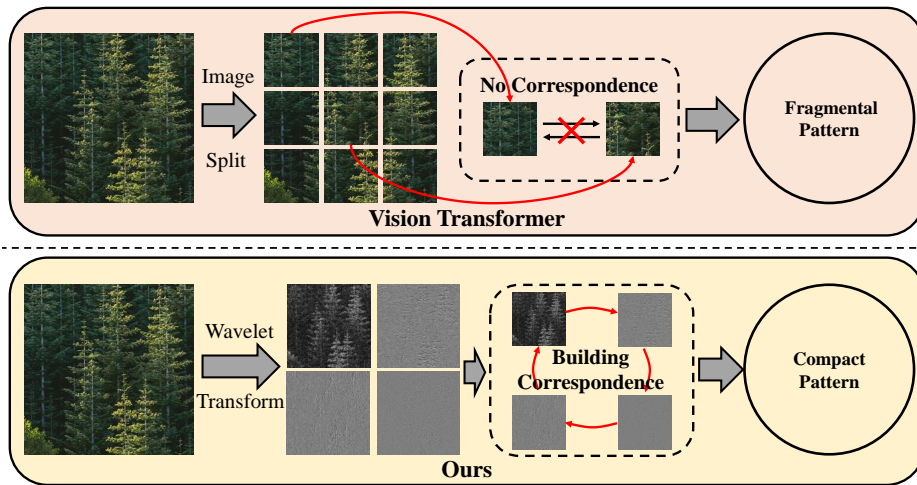


Figure 1: The tokenization strategy in Vision Transformer (ViT) roughly divides the image into patches and breaks the image continuity. We address the **long-range correspondence** on compact yet intact representation by a wavelet sliding-transformer.

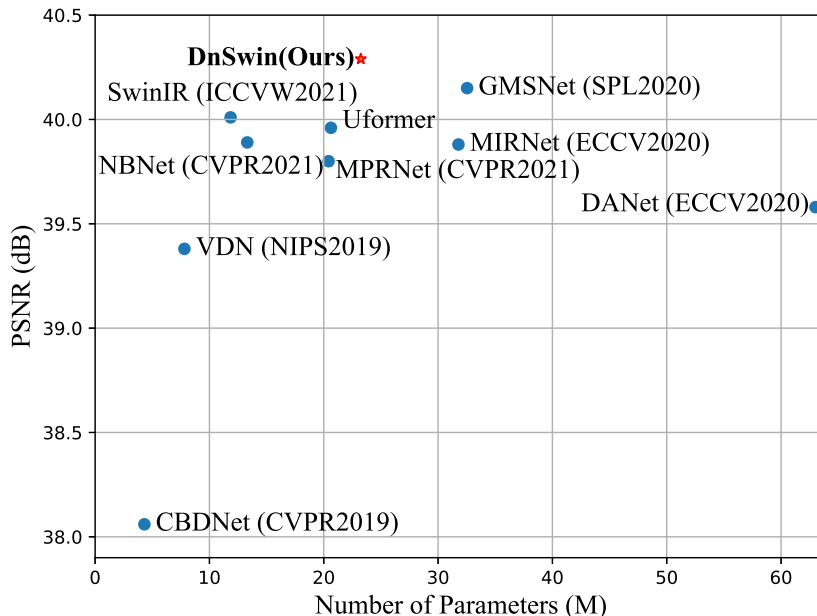


Figure 2: PSNR results v.s. the total number of parameters of different methods for real-world image denoising on DND [6] Benchmark.

Traditional model-based solutions try to explore the image prior knowledge to regularize this essentially ill-posed problem of degradation processing from a Bayesian viewpoint. In the past decades, various methods have been proposed by learning prior knowledge from nonlocal self-similarity [7], sparse representation [8], and total variation [9] models. Although the above methods have shown satisfactory results, they usually suffer from involving too many manually selected features to constrain the image, which makes their optimization process time-consuming and limits their practicality.

Compared with model-based denoising methods, existing learning-based restoration methods [10, 11, 12, 13] address the above problem more efficiently and obtain charming visual quality for handling images with synthetic noise, such as Additive White Gaussian noise (AWGN). However, real-world image denoising remains a challenging task, as the processing steps within the camera systems, such as demosaicing, Gamma correction and compression, are constructed diversely. In recent years, researchers tried to build CNN-based denoisers to handle real-world noisy photographs by modeling real noise [10, 14], obtaining noisy and noise-free image pairs [15, 6], applying unsupervised/self-supervised learning strategy [16, 17]. Typically, CNN-

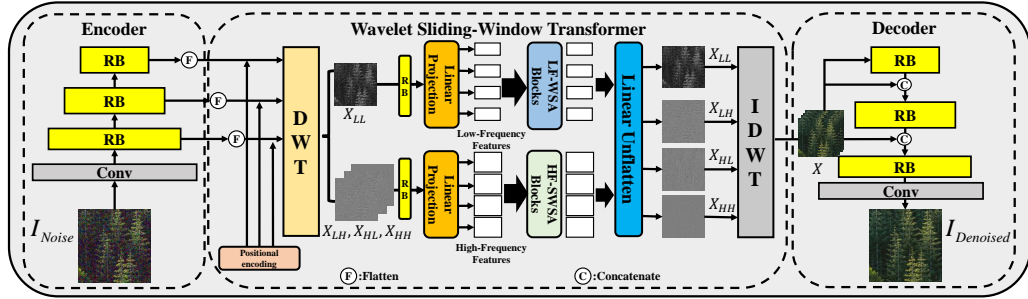


Figure 3: The overall architecture of DnSwin, which consists of Encoder module, Wavelet Sliding-Window Transformer and Decoder module.

based real-world denoising approaches [18, 19] choose ‘UNet’ [20] as their backbone architecture. Nevertheless, reduplicative downsampling operations in UNet cause serious damage to high-frequency information which is consequential for image content preservation.

To address this problem, several recent works [21, 22] have attempted to utilize ViT for image restoration task. However, there are two challenges to use ViT for image restoration. First, the standard ViT structure [23] applies a global-attention mechanism between all tokens. As shown in Figure 1, Vision Transformer (ViT) exhibits a strong ability on capturing long-range dependencies. However, in real-world denoising task, the real-world image is an isolated frame that ViT has to build the dependency on the fragmental patches. ViT-based denoiser realizes the tokenization by cutting the large-size image into patches, which breaks the noise pattern. Second, previous works [24, 25] showed that ViT has a limitation to capture local dependencies, which is essential for image restoration tasks.

Against these issues, we proposed a novel hybrid framework for image denoising, depicted in Figure 3, DnSwin consists of three encoder stages, three decoder stages and Wavelet Sliding-Windows Transformer (WST). In our model, we first utilize a CNN encoder to execute bottom feature encoding from noisy input images. As discrete wavelet transform (DWT) can preserve the information of different frequency bands which are important when recovering images, we apply DWT to achieve the separation of low-frequency features and high-frequency features. Furthermore, we introduce Low-Frequency Windows-based Self-Attention (LF-WSA) and High-Frequency Sliding-Windows-based Self-Attention (HF-SWSA) to build frequency correspondence on compact yet intact representation. Subsequently,

we integrate the multi-frequency sub-bands into features using inverse discrete wavelet transform (IDWT). Finally, we reconstruct the features into denoised images using a CNN decoder.

Extensive experiments are conducted to evaluate DnSwin on real-world denoising. The results on four real-world denoising benchmarks show that DnSwin achieves the state-of-the-art denoising performance on real-world scenes. Especially on Darmstadt Noise Dataset (DND) [6] Benchmark, as shown in Figure 2, our proposed DnSwin achieves obvious improvement over other state-of-the-art methods while utilizing suitable parameters. Generally, our contributions can be summarized as:

- We propose a wavelet ViT architecture for real-world image denoising. The proposed model captures long-range correspondence along frequency sub-band on compact yet intact image content. This strategy disentangles structural information from high- and low-frequency correspondence and provide a better interpretation for ViT-based denoiser.
- We propose Low-Frequency Windows-based Self-Attention (LF-WSA) Block and High-Frequency Sliding-Windows-based Self-Attention (HF-SWSA) Block to make DnSwin intently exact different frequency features, especially the noise features in high-frequency.
- Experimental results demonstrate that our model achieves state-of-the-art performance on the real-world benchmark in terms of PSNR and SSIM.

The rest parts of this paper are organized as follows. Section 2 briefly surveys advances in deep denoising models dealing with additive white Gaussian noise (AWGN) and real-world noise, and the progress in ViT. Section 3 presents the network architecture, and detailed explanations about Low-Frequency Windows-based Self-Attention (LF-WSA) and High-Frequency Sliding-Windows-based Self-Attention (HF-SWSA). In Section 4, we perform experiments to verify the effectiveness and efficiency of DnSwin and compare it with existing state-of-the-art methods. Finally, we conclude our work and propose some future work in Section 5.

## 2. Related Work

**Gaussian Denoising.** As a fundamental low-level image processing challenge, image denoising has been intensively studied for decades. Most of traditional denoising methods can be interpreted within the Maximum A Posteriori (MAP) framework, e.g., total variation [9], sparse representation [8], wavelet coring [26] and nonlocal self-similarity [7]. These methods learn the image prior model parameters in a way of recognition and compact unrolled inference, and also introduce model-guided discriminatory learning. However, these methods tend to over-smooth image details. To this end, Mahdaoui et al. [27] proposed a compressed sensing (CS) reconstruction method that combines the total variation regularization and the non-local self-similarity constraint to achieve a significant improvement in terms of denoising efficiency and visual quality.

Benefit from the success of deep learning, many researchers focus on the exploration of CNN network structure. Advanced architecture designs have achieved very competitive performance in comparison to traditional methods. For instance, Burger et al. [28] trained a plain multi-layer perceptron (MLP) with a large synthetic noise dataset, which achieved comparable results with BM3D. Chen et al. [29] proposed a trainable nonlinear reaction diffusion (TNRD) approach to learn truncated gradient descent inference. Zhang et al. [30] further proposed the denoising convolution network (DnCNN), which composed the model by utilizing batch normalization (BN) [31] and residual connection [32]. While Mao et al. [33] proposed REDNet, a deep fully convolutional encoding-decoding network with symmetric skip connections.

Driven by the advances in self-attention [34], many approaches try to extract the global features of the image by using self-attention mechanism to improve the visual effect. Mei et al. [35] proposed a novel Pyramid Attention module for image restoration, which can capture long-range feature correspondences from a multi-scale feature pyramid. Zhang et al. [36] designed non-local attention blocks to capture global information and pay more attention to the challenging parts, however, it leads to high memory occupation and time consumption.

Nevertheless, the above learning-based denoising approaches are all trained with synthetic noisy datasets, which can only perform well when processing images with additive white Gaussian noise (AWGN), but will be significantly degraded when applied to real-world images. Inspired by the aforementioned works, we proposed a novel hybrid network architecture, which inherits the

superiority of CNN and ViT and demonstrates a stronger generalization ability.

**Real-World Noisy Images.** For real-world noisy images, the noise model is indeed distinct from Addictive White Gaussian Noise(AWGN). Actually, real noise is sophisticated and the camera image signal processing (ISP) pipeline further increases its complexity. As a remedy, existing deep denoisers for handling real-world noisy images usually are trained either by exploiting realistic noise models to synthesize noisy images or acquiring real paired noisy and noise-free images. CBDNet [10] proposed a realistic noise model including heterogeneous Gaussian and ISP pipeline, which is composed of two sub-networks, including noise estimation and non-blind denoising module. Chen et al. proposed GCBD [37] to extract the smaller image with clear background in noisy images, and then incorporating GAN to generate more fake noise samples for training denoising CNN network. RIDNet [38] proposed a single-state denoising network with feature attention for real-world noise reduction. GRDN [39] have won the champions on the sRGB track in NTIRE 2019 [40], it incorporated groups residual dense blocks (GRDBs) and convolutional block attention module (CBAM) for real-world image denoising.

However, the above approaches ignore the correspondence between multi-frequency features, and fail to build the local and global context, therefore the complex noise information inside real-world images cannot be removed well. To this end, DnSwin proposes a Wavelet Sliding-Window Transformer to decompose, extract, and integrate multi-frequency features that achieves the state-of-the-art results on real-world denoising benchmark.

**Vision Transformer.** Transformer [34] has achieved significant performance in natural language processing (NLP). Compared with CNN, the multi-head self-attention and feed-forward MLP layer in Transformer are naturally good at capturing long-range dependencies between words by the global self-attention. Due to the success of Transformer in NLP, there are many attempts to explore the potential of Transformer in computer vision tasks. The pioneering work of ViT [41] gets excellent results compared to state-of-the-art CNNs on image classification by dividing images into  $16 \times 16$  image patches and then stretched them into one-dimensional vectors that were fed into Transformer blocks. Chen et al. [42] proposed TransUnet, a hybrid framework using ViT and UNet based on convolutional operations for medical image segmentation. Because of the limitation of ViT in capturing local context, several works try to add convolutional layers into the multi-head

self-attention [24, 43] and the feed-forward network [44, 25]. Liu et al. [45] proposed Swin Transformer, which significantly reduces the computational cost of ViT by using the shifted windows-based multi-head attentions.

Besides image classification and segmentation, Transformer also shows the potential in image restoration tasks. Yang et al. [21] proposed TTSR, introduce the ViT-based architecture into image restoration tasks firstly. They used a cross-scale feature integration module to stack texture transformer, which achieved a more powerful feature transformer. IPT [22] exploits the potential of pre-training and transfer learning with a shared ViT-based backbone. To address multiple image restoration tasks (e.g., super-resolution, denoising, and deraining), it employs each head and each tail for each image restoration task separately. However, the above approaches still need large-scale referenced data for training. Differently, DnSwin is able to achieve surprising performance with limited training sample numbers by incorporating wavelet CNN and ViT combination based architecture.

### 3. Methodology

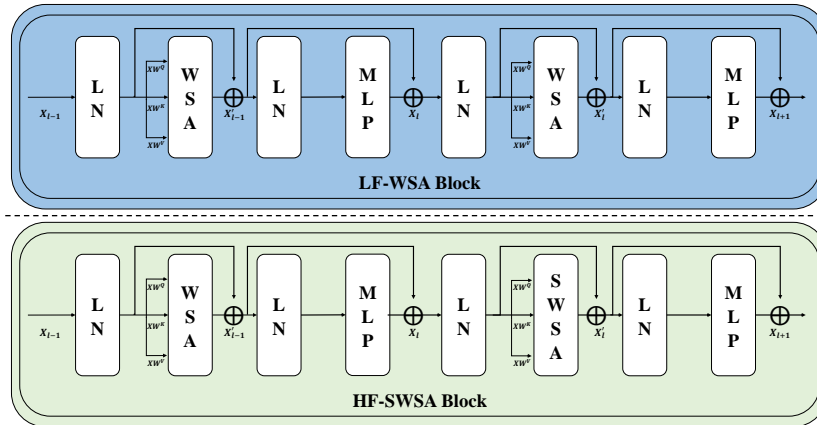


Figure 4: The detail of Low-Frequency Windows-based Self-Attention (LF-WSA) Block and High-Frequency Sliding-Windows-based Self-Attention (HF-SWSA) Block.

In this section, we will present the real-world image denoising network based on DnSwin. We first briefly describe the overall architecture details of DnSwin. Then, we provide more detailed explanations about bottom feature acquisition, Wavelet Sliding-Window Transformer with three sub-modules

(i.e., Wavelet Feature Decomposition, Frequency Correspondence Building and Multi-frequency Integration) and reconstruction, respectively.

### 3.1. Overall Architecture Details

As shown in Figure 3, DnSwin consists of three components: Encoder module, Wavelet Sliding-Window Transformer and Decoder module. Specifically, the feature encoder module uses convolution layers to extract bottom features:

$$F_b^i = H_E(I_{noisy}), \quad (2)$$

where  $F_b^i$  denotes the extracted bottom feature,  $i$  is the index of layer,  $H_E$  is the function of feature encoder, and  $I_{noisy}$  refers to the noisy image. Then, we use Wavelet Sliding-Window Transformer (WSWT) to separate different frequency information from bottom feature and build the frequency dependencies:

$$F_d^i = H_W(F_b^i), \quad (3)$$

where  $H_W$  is the function of WSWT and  $F_d^i$  denotes the deep feature extracted by WSWT. The feature decoder uses convolution layers and concatenation operator to fuse hierarchical features and reconstruct the image:

$$F_r^{i-1} = H_D(Concat(F_d^i \uparrow, F_d^{i-1})), \quad (4)$$

where  $F_r^i$  denotes the reconstruction feature from decoder, when  $i = 0$ ,  $F_r^0 = I_{Denoised}$  refers to the denoised image,  $H_D$  is the function of feature decoder, and  $\uparrow$  is the upasampling operation.

### 3.2. Bottom Feature Acquisition

We utilize the encoder to execute bottom feature encoding from noisy input images. The feature encoder contains a convolutional layer and three stages of Residual Blocks (RB). Each Residual Block consists of three convolutional layers and two leaky ReLU layers. Specifically, given a noisy image  $I_{noisy} \in \mathbb{R}^{3 \times H \times W}$  ( $H$  and  $W$  are the input image height and width, respectively), we firstly apply a  $3 \times 3$  convolutional layer to extract features  $\mathbf{X}^0 \in \mathbb{R}^{C \times H \times W}$ , where  $C$  denotes the number of output channels. Next, different stages feature maps  $\mathbf{X}^l$  produced by Residual Blocks [32] can be formally expressed as:

$$\begin{aligned} \mathbf{X}^0 &= \text{Conv}(I_{noisy}), \\ \mathbf{X}^i &= H_{RB}(\mathbf{X}^{i-1}) \downarrow. \end{aligned} \quad (5)$$

where Conv is the convolutional operation,  $\{\mathbf{X}^1, \mathbf{X}^2, \dots, \mathbf{X}^i\} \in \mathbb{R}^{2^i C \times \frac{H}{2^i} \times \frac{W}{2^i}}$  denotes the  $i$ -th stage output feature maps, and  $H_{RB}(\cdot)$  is the function of residual block. In the downsampling layer  $\downarrow$ , we use  $4 \times 4$  convolution with stride 2, and the number of feature maps is doubled in order to reduce the information loss while each downsampling.

### 3.3. Wavelet Sliding-Window Transformer

Since the typical convolutional operator owns a local receptive field, the feature encoder fails to capture the long-range dependency of pixels. To this end, we propose the Wavelet Sliding-Window Transformer, which introduces the multi-frequency self-attention mechanism for long-range contextual extracting and correspondence modeling.

#### 3.3.1. Wavelet Feature Decomposition

Discrete Wavelet Transform (DWT) provides a signal decomposition with attractive time-frequency localization properties that has the potential to decompose feature map into different frequencies for further processing. More specifically, DWT decomposes an image into a low-frequency sub-band and three high-frequency sub-bands. The low-frequency sub-band contains the detail information, while the high-frequency sub-band contains the structure information. Given the feature maps  $\mathbf{X} = \{\mathbf{X}^1, \mathbf{X}^2, \dots, \mathbf{X}^i\}$  obtained by feature acquisition, we first flatten them into patches and apply learnable positional encoding for spatial information modeling, and then use DWT to decompose the patches into different frequencies intervals by the following equations:

$$\begin{cases} \mathbf{X}_{LL} = (\mathbf{f}_{LL} * \mathbf{X}) \downarrow_2, \\ \mathbf{X}_{LH} = (\mathbf{f}_{LH} * \mathbf{X}) \downarrow_2, \\ \mathbf{X}_{HL} = (\mathbf{f}_{HL} * \mathbf{X}) \downarrow_2, \\ \mathbf{X}_{HH} = (\mathbf{f}_{HH} * \mathbf{X}) \downarrow_2, \end{cases} \quad (6)$$

where the sub-bands  $\{\mathbf{X}_{LL}, \mathbf{X}_{LH}, \mathbf{X}_{HL}, \mathbf{X}_{HH}\}$  denote the approximation, horizontal detail, vertical detail and diagonal detail of the feature using the Harr wavelet transform, respectively.  $*$  is convolution operator, and  $\downarrow_2$  means the standard downsampling operator with factor 2. The low-pass filter  $\mathbf{f}_{LL}$  and three typical high-pass filters  $\mathbf{f}_{LH}$ ,  $\mathbf{f}_{HL}$ ,  $\mathbf{f}_{HH}$  are defined as:

$$\begin{aligned} \mathbf{f}_{LL} &= \begin{bmatrix} 1 & 1 \\ 1 & 1 \end{bmatrix}, & \mathbf{f}_{LH} &= \begin{bmatrix} -1 & -1 \\ 1 & 1 \end{bmatrix}, \\ \mathbf{f}_{HL} &= \begin{bmatrix} -1 & 1 \\ -1 & 1 \end{bmatrix}, & \mathbf{f}_{HH} &= \begin{bmatrix} 1 & -1 \\ -1 & 1 \end{bmatrix}. \end{aligned} \quad (7)$$

After we get  $\{\mathbf{X}_{LL}, \mathbf{X}_{LH}, \mathbf{X}_{HL}, \mathbf{X}_{HH}\}$ , we divide them into low-frequency sub-band  $\mathbf{X}_{LL}$  and high-frequency sub-bands  $\{\mathbf{X}_{LH}, \mathbf{X}_{HL}, \mathbf{X}_{HH}\}$  and use residual blocks to extract the local features of the different frequency sub-bands.

In order to build correspondence between the different frequencies sub-bands, we use Low-Frequency Windows-based Self-Attention (LF-WSA) and High-Frequency Sliding-Windows-based Self-Attention (HF-SWSA) to extract global feature and capture long-range dependencies.

### 3.3.2. Building Frequency Correspondence via Sliding-Window

The details of Low-Frequency Windows-based Self-Attention (LF-WSA) and High-Frequency Sliding-Windows-based Self-Attention (HF-SWSA) are shown in Figure 4, which benefits from the self-attention in Transformer to capture long-range dependencies, and also builds frequency correspondence between all sub-bands.

As shown in Figure 4, each High-Frequency Sliding-Windows-based Self-Attention block consists of LayerNorm (LN) [46] Layer, the multi-head Windows-based Self Attention (WSA) unit, the multi-head Sliding-Windows-based Self Attention (SWSA) unit and 2-layer Multi-Layer Perceptron (MLP) with GELU non-linearity activation function, and LF-WSA Block is modified from HF-SWSA Block by replacing a SWSA unit with WSA unit. The computation of a HF-SWSA block is represented as:

$$\begin{aligned}
 \mathbf{X}'_l &= \text{WSA}(\text{LN}(\mathbf{X}_{l-1})) + \mathbf{X}_{l-1}, \\
 \mathbf{X}_l &= \text{MLP}(\text{LN}(\mathbf{X}'_l)) + \mathbf{X}'_l, \\
 \mathbf{X}'_{l+1} &= \text{SWSA}(\text{LN}(\mathbf{X}_l)) + \mathbf{X}_l, \\
 \mathbf{X}_{l+1} &= \text{MLP}(\text{LN}(\mathbf{X}'_{l+1})) + \mathbf{X}'_{l+1}.
 \end{aligned} \tag{8}$$

where  $\mathbf{X}'_l$  and  $\mathbf{X}_l$  represent the outputs of the WSA and SWSA unit and the MLP module in  $l$ -th layer, respectively. Next, we introduce the details of WSA and SWSA.

**Windows-based Self Attention (WSA).** Given a feature map  $\mathbf{X} \in \mathbb{R}^{C \times H \times W}$ , we first split it into non-overlapping windows with the windows size of  $M \times M$ , and get the transposed features  $\{\mathbf{X}^1, \mathbf{X}^2, \dots, \mathbf{X}^N\} \in \mathbb{R}^{M^2 \times C}$ ,  $N = HW/M^2$  from each window. Then, we apply self-attention mechanism on  $\mathbf{X}^N$ . Suppose the head number is  $h$  and the head dimension is  $d = C/h$ . The

workflow of WSA can be formulated as:

$$\begin{aligned} \mathbf{X} &= \{\mathbf{X}^1, \mathbf{X}^2, \dots, \mathbf{X}^N\}, N = HW/M^2, \\ \mathbf{Y}_k^n &= \text{Attention}(\mathbf{X}^n \mathbf{W}_k^Q, \mathbf{X}^n \mathbf{W}_k^K, \mathbf{X}^n \mathbf{W}_k^V), n = 1, \dots, N, \\ \hat{\mathbf{X}}_k &= \{\mathbf{Y}_k^1, \mathbf{Y}_k^2, \dots, \mathbf{Y}_k^N\}, \end{aligned} \quad (9)$$

where  $\mathbf{W}_k^Q, \mathbf{W}_k^K, \mathbf{W}_k^V \in \mathbb{R}^{C \times d}$  denote the query, key and value window-based projection matrices for the  $k$ -th head, respectively. The outputs for all heads  $\{\hat{\mathbf{X}}_1, \hat{\mathbf{X}}_2, \dots, \hat{\mathbf{X}}_k\}$  are concatenated and linearly projected to get the final result. Following the previous works, the self-attention mechanism can be formulated as:

$$\begin{aligned} &\text{Attention}(\mathbf{X}\mathbf{W}^Q, \mathbf{X}\mathbf{W}^K, \mathbf{X}\mathbf{W}^V) \\ &= \text{SoftMax}\left(\frac{(\mathbf{X}\mathbf{W}^Q)(\mathbf{X}\mathbf{W}^K)^T}{\sqrt{d}} + B\right)(\mathbf{X}\mathbf{W}^V), \end{aligned} \quad (10)$$

where  $B$  denotes the relative position bias, and values in  $B$  are taken from the bias matrix  $\hat{B} \in \mathbb{R}^{(2M-1) \times (2M-1)}$ .

As shown in Figure 3, for low-frequency sub-band, we use Low-Frequency Windows-based Self-Attention Blocks to extract features to reduce the computational cost. For high-frequency sub-bands, we replace Low-Frequency Windows-based Self-Attention Blocks with High-Frequency Sliding-Windows-based Self-Attention Blocks to further extract the noise features, as noise belongs to high-frequency feature.

***Sliding-Windows-based Self Attention (SWSA)***. Since WSA performs self-attention within each window and lacks cross-window connectivity, which limits its modeling capabilities. Based on WSA, we introduce sliding mechanism to build connections across windows called SWSA.

As shown in Figure 5(a), given a feature map  $\mathbf{X} \in \mathbb{R}^{C \times H \times W}$ , we use the same window partitioning strategy as WSA. Then, we slide all windows to the bottom-right by  $(\lfloor \frac{M}{2} \rfloor, \lfloor \frac{M}{2} \rfloor)$  from the top-left pixel, through which the red part on the left side and the blue part on the top in the feature move to the right and the bottom, respectively, as shown in Figure 5(b). The SWSA is divided into the following parts: 1) The sub-windows consisting entirely of yellow overlapping area are similar to Eq. (10). 2) The sub-windows consisting of the different color areas are illustrated in the bottom of Figure 5. Specifically, the color area (yellow, blue) in the feature will remain the same color after applying self-attention mechanism on the purple feature. On the contrary, the green area obtained from the matrix calculation of the yellow

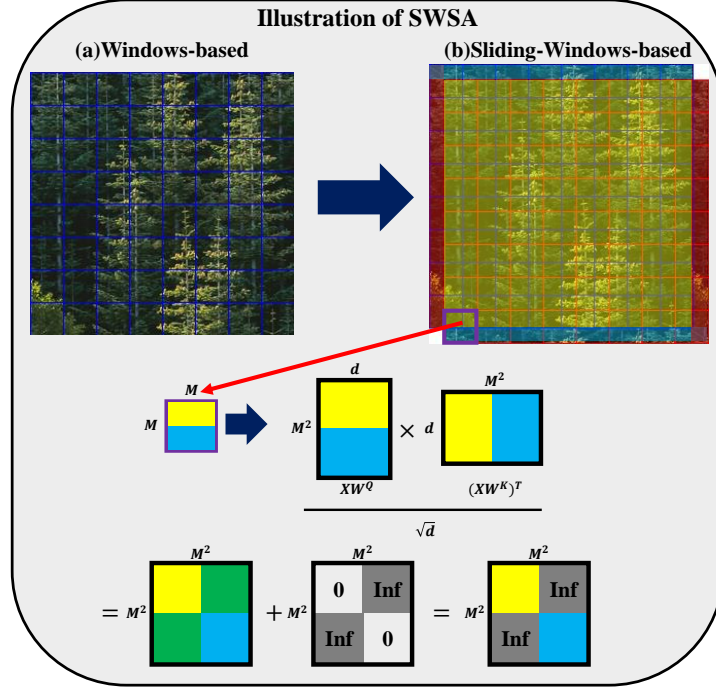


Figure 5: The illustration of Sliding-Windows-Based Self-Attention (SWSA).

and blue areas is the meaningless similarity, so we apply mask mechanism on it to restrict self-attention computation within each sub-window.

**Sliding Mechanism.** Benefited from sliding mechanism, three high-frequency sub-bands build correspondence that can effectively extract different noise features in high frequency. More specifically, given the low-frequency feature map  $\mathbf{X}_{LL}$  and high-frequency feature maps  $\{\mathbf{X}_{LH}, \mathbf{X}_{HL}, \mathbf{X}_{HH}\}$ , we extract deep feature from LF-WSA and HF-SWSA as:

$$\begin{aligned} \hat{\mathbf{X}}_{LL} &= H_{LF}(\mathbf{X}_{LL}), \\ \{\hat{\mathbf{X}}_{LH}, \hat{\mathbf{X}}_{HL}, \hat{\mathbf{X}}_{HH}\} &= H_{HF}(\{\mathbf{X}_{LH}, \mathbf{X}_{HL}, \mathbf{X}_{HH}\}). \end{aligned} \quad (11)$$

where  $H_{LF}(\cdot)$  and  $H_{HF}(\cdot)$  are the LF-WSA and HF-SWSA blocks, respectively.

Furthermore, WSA can significantly reduce the computational cost compared with global self-attention. Given the feature map  $\mathbf{X} \in \mathbb{R}^{C \times H \times W}$  and window size  $M$ , the computational complexity of global Multi-head Self At-

tention (MSA) and WSA are:

$$\begin{aligned} O(\text{MSA}) &= 4HWC^2 + 2(HW)^2C, \\ O(\text{WSA}) &= 4HWC^2 + 2M^2HWC. \end{aligned} \tag{12}$$

**Difference to Swin-Transformer.** In Swin Transformer [45], tokenization is a necessary step, which is inappropriate for large-size image denoising. Suppose we simply apply Swin-Transformer into real-world denoising task, the full-size image will be cut into fragmental patches, which breaks the image continuity and noise pattern undoubtedly. In the proposed DnSwin, we combine wavelet operator with Transformer, which preserves compact yet intact feature representation. Moreover, we investigate sliding-transformer to build a long-range correspondence along frequency sub-band on unbroken image content. This strategy disentangles structural information from high- and low-frequency correspondence for better interpretation of real-world image denoising.

### 3.3.3. Multi-frequency Integration

As shown in Figure 3, since we design DnSwin as a hierarchical architecture, the LF-WSA Blocks at low-frequency feature map  $\mathbf{X}_{LL}$  work on larger receptive fields and are sufficient to learn long-range dependencies. And the Blocks at high-frequency feature maps  $\{\mathbf{X}_{LH}, \mathbf{X}_{HL}, \mathbf{X}_{HH}\}$  learn the different noise features and build the connection between three high-frequency sub-bands.

Still, we need to build correspondence between the low-frequency sub-band and high-frequency sub-bands. Therefore, we propose to apply Inverse Discrete Wavelet Transform (IDWT) to the integration of multi-frequency sub-bands. Specifically, we first get the outputs  $\hat{\mathbf{X}}_{LL}$  and  $\{\hat{\mathbf{X}}_{LH}, \hat{\mathbf{X}}_{HL}, \hat{\mathbf{X}}_{HH}\}$  of LF-WSA Blocks and HF-SWSA Blocks as described by Eq. (11), then we unflatten and expand them to feature maps  $\{\hat{\mathbf{X}}_{LL}, \hat{\mathbf{X}}_{LH}, \hat{\mathbf{X}}_{HL}, \hat{\mathbf{X}}_{HH}\}$ . Finally, the multi-frequency feature maps  $\{\hat{\mathbf{X}}_{LL}, \hat{\mathbf{X}}_{LH}, \hat{\mathbf{X}}_{HL}, \hat{\mathbf{X}}_{HH}\}$  are integrated by IDWT, which can reconstruct the original features from the wavelet sub-

bands accurately. The operation of IDWT is defined as follows:

$$\left\{ \begin{array}{l} \hat{\mathbf{X}}(2i-1, 2j-1) = (\hat{\mathbf{X}}_{LL}(i, j) - \hat{\mathbf{X}}_{LH}(i, j) \\ \quad - \hat{\mathbf{X}}_{HL}(i, j) + \hat{\mathbf{X}}_{HH}(i, j))/4, \\ \hat{\mathbf{X}}(2i-1, 2j) = (\hat{\mathbf{X}}_{LL}(i, j) - \hat{\mathbf{X}}_{LH}(i, j) \\ \quad + \hat{\mathbf{X}}_{HL}(i, j) - \hat{\mathbf{X}}_{HH}(i, j))/4, \\ \hat{\mathbf{X}}(2i, 2j-1) = (\hat{\mathbf{X}}_{LL}(i, j) + \hat{\mathbf{X}}_{LH}(i, j) \\ \quad - \hat{\mathbf{X}}_{HL}(i, j) - \hat{\mathbf{X}}_{HH}(i, j))/4, \\ \hat{\mathbf{X}}(2i, 2j) = (\hat{\mathbf{X}}_{LL}(i, j) + \hat{\mathbf{X}}_{LH}(i, j) \\ \quad + \hat{\mathbf{X}}_{HL}(i, j) + \hat{\mathbf{X}}_{HH}(i, j))/4, \end{array} \right. \quad (13)$$

where  $\hat{\mathbf{X}}(i, j)$  is the  $(i, j)$ -th index of  $\hat{\mathbf{X}}$ . Different stage feature maps  $\hat{\mathbf{X}} = \{\hat{\mathbf{X}}^1, \hat{\mathbf{X}}^2, \dots, \hat{\mathbf{X}}^i\}$  are obtained by Eq. (13).

Benefited from IDWT, the multi-frequency sub-bands can be completely integrated into features  $\hat{\mathbf{X}}^i$  that have the same dimension as the input features  $\mathbf{X}^i$ . Moreover, the **correspondence** between the low-frequency sub-band and high-frequency sub-bands has been established, which disentangles valuable structural from high- and low-frequency correspondence for better performance of real-world image denoising.

### 3.4. Reconstruction

The reconstruction phrase employs three stages of Residual Blocks and a convolutional layer for feature reconstruction. The convolutional layers are adopted in the reconstruction phase for two aspects: 1) although Transformer can be considered as a specific instantiation of spatially varying convolution [47, 48], convolutional layers with spatially invariant filters can enhance the translational equivalence of DnSwin. 2) the residual blocks and concatenation operator aggregate the different levels of features.

We use  $2 \times 2$  transposed convolution with stride 2 for the upsampling layer. The upsampling layers double the size of the feature maps and reduce half of the channels number. After the upsampling operation, we concatenate  $\hat{\mathbf{X}}^{i-1}$  and  $\hat{\mathbf{X}}^i$  together to reduce the impact of spatial information caused by downsampling. The denoised image  $I_{Denoised}$  can be reconstructed by the

following equation:

$$\begin{cases} \hat{\mathbf{X}}^i = H_{RB}(\hat{\mathbf{X}}^i), \\ \mathbf{X}^{\hat{i}-1} = H_{RB}(\text{Concat}(\hat{\mathbf{X}}^i \uparrow, \mathbf{X}^{\hat{i}-1})), \\ \dots, \\ \hat{\mathbf{X}}^1 = H_{RB}(\text{Concat}(\hat{\mathbf{X}}^2 \uparrow, \hat{\mathbf{X}}^1)), \\ I_{Denoised} = \text{Conv}(\hat{\mathbf{X}}^1). \end{cases} \quad (14)$$

where  $\uparrow$  is the upsampling operation.

### 3.5. Loss Function

Instead of using  $\mathcal{L}_1$  loss, our model is optimized with the robust Charbonnier loss [49] to better handle outliers and improve the performance. The Charbonnier loss is defined as follows:

$$\mathcal{L}_{char} = \sqrt{\|I_{Denoised} - I_{GT}\|^2 + \varepsilon^2} \quad (15)$$

where  $I_{GT}$  represents the ground-truth image, and  $\varepsilon$  is empirical value. Compared with  $\mathcal{L}_1$  loss, using  $\mathcal{L}_{char}$  will make the model more robust. In Section 4.4, we will show that using  $\mathcal{L}_{char}$  loss is superior to using  $\mathcal{L}_1$  loss.

## 4. Experiments

In this section, we first describe the experiment settings, including the training and testing settings and implementation details. Then, we compare our model with state-of-the-art methods on three real-world image denoising benchmarks (*e.g.*, SIDD validation dataset, SIDD benchmark and DND benchmark). Finally, we evaluate the contributions of different DnSwin components and parameters through an ablation study and analyze the efficiency of our model.

### 4.1. Dataset and Evaluation Protocols

We use following two real-world noisy-clean datasets for comprehensive comparisons to validate our model:

- *SIDD* [15] consists of 30000 LR-HR image pairs, which are collected under different lighting conditions using five representative smartphone cameras and generated their ground truth images. For fast training and

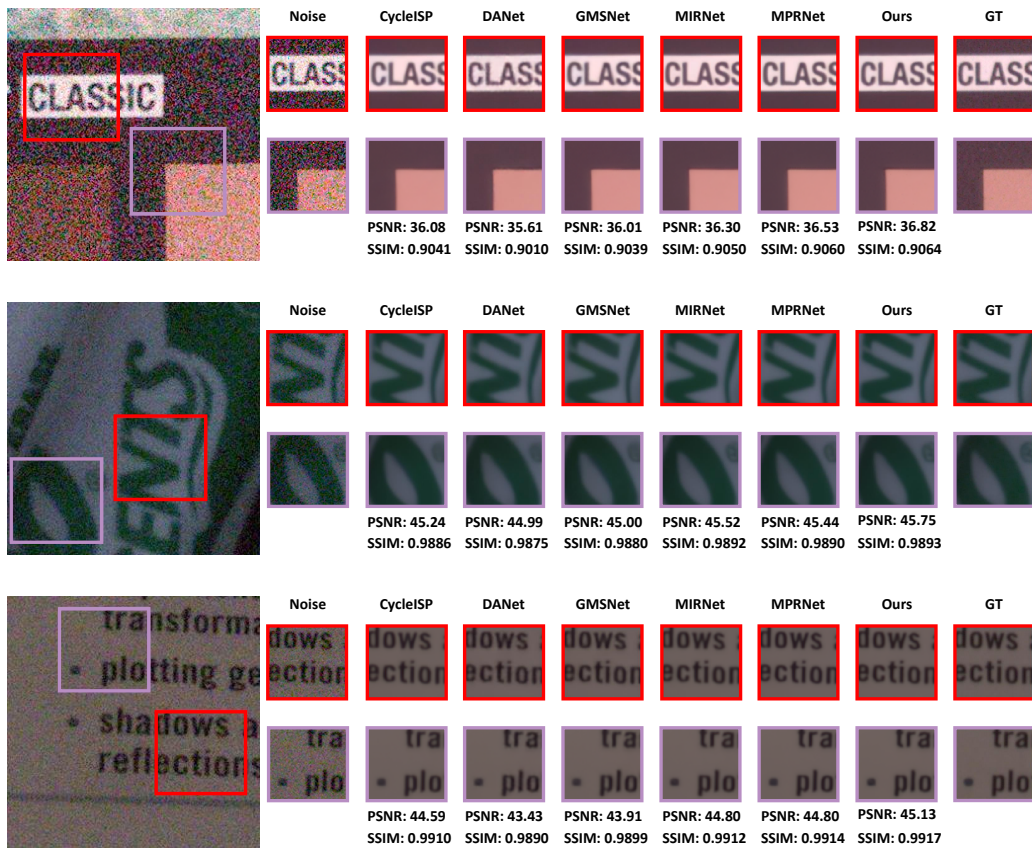


Figure 6: Comparison with state-of-the-art methods on real noisy images from SIDD Validation Dataset [15]. (**Zoom in for best view**)

evaluation, we using the SIDD-Medium dataset (320 image pairs) for training, and evaluated on the SIDD validation set and SIDD benchmark<sup>1</sup>.

- *DND* [6] consists of 50 pairs of real noisy images and corresponding ground truth images that were captured with consumer-grade cameras of differing sensor sizes. But *DND*<sup>2</sup> does not provide any additional training data for fine-tuning denoising networks and can only be evaluated online.

<sup>1</sup><https://www.eecs.yorku.ca/kamel/sidd/benchmark.php>

<sup>2</sup>[https://noise.visinf.tu-darmstadt.de/benchmark/#results\\_srgb](https://noise.visinf.tu-darmstadt.de/benchmark/#results_srgb)

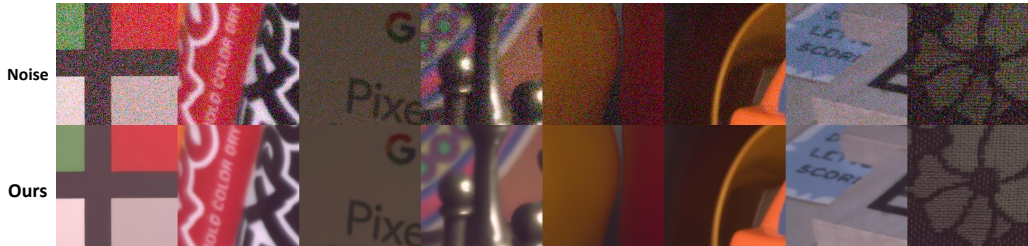


Figure 7: The visual results of DnSwin provided by SIDD Benchmark online testing. Notice that there are no Ground Truth image and visual results of other state-of-the-art methods for comparison. (**Zoom in for best view**)

In evaluation protocols, we adopted Peak Signal-to-Noise Ratio (PSNR) and Structural Similarity Image measurement (SSIM) to verify our model, because they are the most commonly used evaluation metrics in image restoration, as they focus on pixel fidelity.

#### 4.2. Implementation Details and Competing Methods

Following the common training of GMSNet [50], we use the Adam optimizer [51] with  $\beta_1 = 0.9$  and  $\beta_2 = 0.999$  to train our framework. To improve the trade-off between the size of input patches and available computing power, we set the batch size to 16 and the image patch size to  $128 \times 128$ . The initial learning rate is  $2 \times 10^{-4}$ . We employ the cosine decay strategy to decrease the learning rate to  $1 \times 10^{-6}$ . For all experiments, we use flip and random rotation with angles of  $90^\circ$ ,  $180^\circ$  and  $270^\circ$  for data augmentation. For Low-Frequency Windows-based Self-Attention (LF-WSA) and High-Frequency Sliding-Windows-based Self-Attention (HF-SWSA) blocks, we set the window size  $M = 8$ . All the experiments are carried out in the Linux and Pytorch (1.4.0) environment running on 2 NVIDIA Tesla V100 GPUs server. And the Nvidia CUDA 10.2 and cuDNN are utilized to accelerate the GPU computation. We train 6000 epochs for DnSwin, which took about four days.

To prove the efficiency and superiority of DnSwin, we compare it with the state-of-the-art approaches on real-world image denoising task. In particular, we evaluate its real-world image denoising performance on three test sets, SIDD Validation dataset [15], SIDD Benchmark and DND Benchmark, respectively.

**SIDD Validation Dataset and SIDD Benchmark.** For SIDD validation dataset and SIDD benchmark, we follow the setting of DANet [18] that

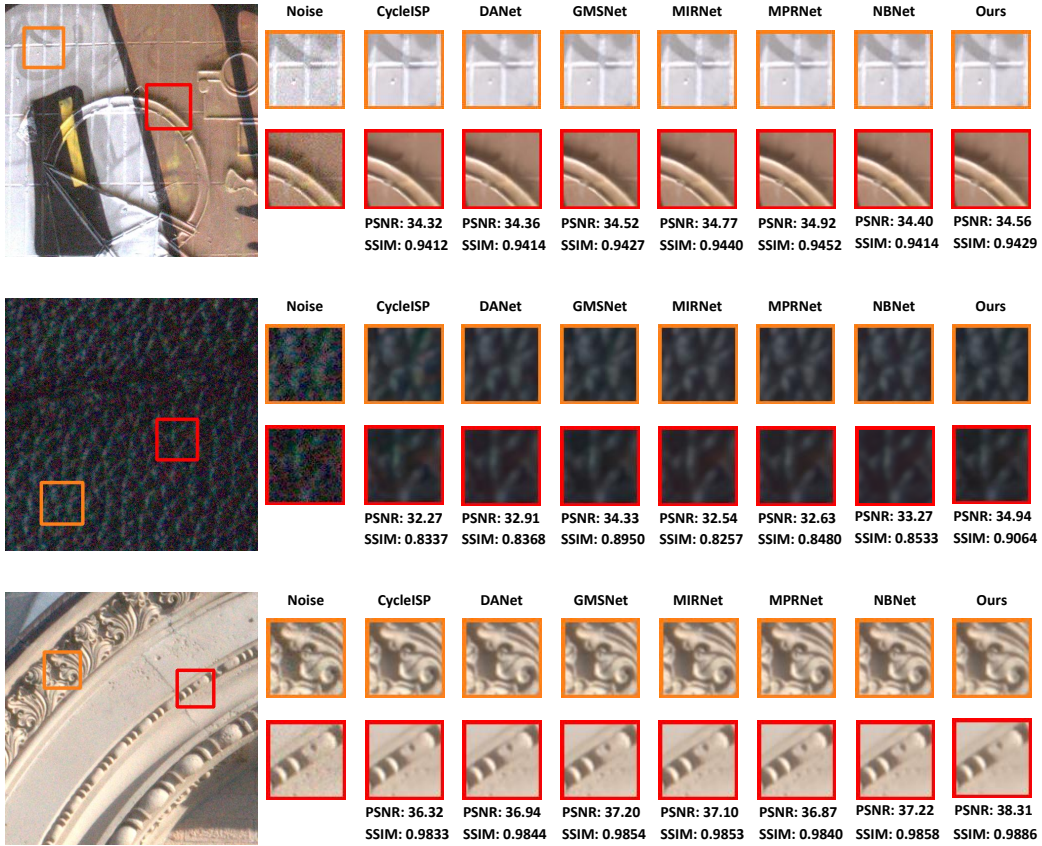


Figure 8: Comparison with state-of-the-art methods on real noisy images from DND Benchmark [6]. Notice that there is no Ground Truth image provided by DND Benchmark. (**Zoom in for best view**)

only uses SIDD-Medium dataset for training. We compare our method with the previous state-of-the-art methods, including CBDNet [10], VDN [11], DANet [18], MIRNet [52], CycleISP [53], MPNet [54], NBNet [19] and GMSNet [50]. It should be noted that there is no official test script available for the corresponding test, so there are fewer baselines for comparison on SIDD Benchmark.

**DND.** For DND benchmark, we trained our model on SIDD-Medium dataset and synthesized noisy images provided by GMSNet [50] for fair comparison. The synthesized noisy images are generated by DIV2K [57]. The high-resolution images in DIV2K are cropped into non-overlapping image patches and then add noise to these patches. We randomly sample 320 im-

Methods	PSNR $\uparrow$	SSIM $\uparrow$	Parameters
CBDNet [10]	30.78	0.801	4.31M
VDN [11]	39.28	0.956	7.81M
DANet [18]	39.47	0.957	63.01M
MIRNet [52]	39.72	0.959	31.18M
CycleISP [53]	39.52	0.957	-
MPRNet [54]	39.71	0.958	20.42M
NBNet [19]	39.75	<u>0.959</u>	13.31M
GMSNet [50]	39.63	0.956	32.54M
Uformer [55]	<u>39.77</u>	<u>0.959</u>	20.63M
SwinIR [56]	<u>39.77</u>	0.958	11.85M
Ours	<b>39.80</b>	<b>0.960</b>	23.24M

Table 1: Quantitative results on SIDD validation dataset [15].

Methods	PSNR $\uparrow$	SSIM $\uparrow$	Parameters
CBDNet [10]	33.28	0.868	4.31M
VDN [11]	39.26	0.955	7.81M
DANet [18]	39.43	0.956	63.01M
GMSNet [50]	<u>39.51</u>	<u>0.958</u>	32.54M
Ours	<b>39.65</b>	<b>0.959</b>	23.24M

Table 2: Quantitative results on SIDD benchmark [15].

age patches from SIDD-Medium dataset and 100 image patches from the synthetic noisy dataset for each iteration in training. We used the same baseline as SIDD validation dataset for comparison.

#### 4.3. Quantitative and Qualitative Comparisons

**SIDD Validation Dataset.** As depicted in Table 1, the results indicate that our model exhibits better performance against all the state-of-the-art methods. For instance, our method performs favorably against the recently developed state-of-the-art method SwinIR [56], where the PSNR and SSIM of the proposed results are 0.03 dB and 0.001 higher than SwinIR, which justify the effectiveness of DnSwin. Compare with DANet [18] used generative

Methods	PSNR $\uparrow$	SSIM $\uparrow$	Parameters
CBDNet [10]	38.06	0.942	4.31M
VDN [11]	39.38	0.952	7.81M
DANet [18]	39.58	0.955	63.01M
MIRNet [52]	39.88	0.956	31.18M
CycleISP [53]	39.56	0.956	-
MPRNet [54]	39.80	0.954	20.42M
NBNet [19]	39.89	0.955	13.31M
GMSNet [50]	<u>40.15</u>	<u>0.961</u>	32.54M
Uformer [55]	39.96	0.956	20.63M
SwinIR [56]	40.01	0.958	11.85M
Ours	<b>40.29</b>	<b>0.962</b>	23.24M

Table 3: Quantitative results on DND benchmark [6].

Method	VDN	DANet	MIRNet	SwinIR	Ours
Time(frame/s)	0.1502	<u>0.0907</u>	0.1524	0.4726	<b>0.0847</b>
Parameters	7.81M	63.01M	31.78M	11.85M	23.24M

Table 4: Efficiency analysis on  $256 \times 256$  image of SIDD validation dataset [15].

adversarial network [58], our model still achieves 0.33 dB improvement on PSNR index. Also, we present the visual comparison in Figure 6. It can be observed that our model recovers relatively sharper and clearer images than the other methods, and is therefore more faithful to the ground truth, which verifies the effectiveness of the local dependencies captured by CNN and the long-range dependency of pixels captured by Wavelet Sliding-Window Transformer.

**SIDD Benchmark.** In Table 2, we present the quantitative comparison on SIDD Benchmark. It shows that our model still achieves first place over all indexes. Our model surpassed the prior state-of-the-art GMSNet [50] by 0.14 dB in PSNR and 0.001 in SSIM. Some visual results of DnSwin provided by online server testing are shown in Figure 7. The visual results show that DnSwin can not only successfully remove the noise but also preserve the texture details. It should be noted that the online server does not pro-

vide Ground Truth and visual results of other state-of-the-art methods for comparison.

**DND Benchmark.** As depicted in Table 3, our model achieves a significant improvement over other state-of-the-art methods. Compared with MPRNet [54], our model demonstrates a performance gain of 0.49 dB in PSNR and 0.008 in SSIM, which justifies that building frequency correspondence via sliding-window makes our model more robust in handling the information of different frequencies. Although DANet enjoys much more parameter numbers, our model achieves 0.71 dB gain with PSNR index. Compared with the ViT-based methods, Uformer [55] and SwinIR [56], our model outperforms them by a PSNR margin of up to 0.30dB. The qualitative results depicted in Figure 8 verify that our model obtains significant visual quality improvement over CycleISP with realistic texture and clear structure.

**Efficiency Analysis.** Despite achieving competitive results in quantitative comparisons, our model still gives an outstanding running efficiency. The comparison in Table 4 shows that our model achieves competing efficiency. Though VDN [11] has the fewest parameters, the test noisy image has to be fed in two networks separately to get the final denoised image, which seriously reduces the inference speed. Compared with MIRNet [52], our model has nearly  $2\times$  running efficiency and significant restoration quality improvement. Compared with DANet [18], our model achieves obvious quantitative promotion with similar time consumption. Although SwinIR [56] has less parameters, it has the worst running efficiency due to the computational complexity of self-attention mechanism.

#### 4.4. Ablation Study

In this section, we first make ablation study on the ‘sliding mechanism’, ‘Convolution + Transformer’ and ‘Wavelet + Transformer’ to justify the effectiveness of our proposed components, respectively. Moreover, we make more ablation studies on the filter number, window size, loss function and using the auxiliary training dataset. All the ablation experiments are evaluating on DND Benchmark.

**Effects of Sliding Mechanism.** We conduct an ablation study on the sliding mechanism and present the experimental results. As depicted in Table 5, ‘Ours w/o LF-WSA’ achieves a 0.05 dB improvement, 0.002 SSIM gain and similar parameter number compared with ‘Ours w/o HF-SWSA’, which justify the effectiveness of sliding mechanism in real-world denoising. Moreover, compared with ‘Ours w/o HF-SWSA’, ‘Ours Full’ demonstrates

Test Set	DND [6]		
Metric	PSNR $\uparrow$	SSIM $\uparrow$	Parameters
Ours w/o LF-WSA	40.08	0.960	22.8M
Ours w/o HF-SWSA	40.03	0.958	22.7M
Ours Full	<b>40.29</b>	<b>0.962</b>	23.2M

Table 5: Ablation study on the effectiveness of sliding mechanism.

Test Set	DND [6]		
Metric	PSNR $\uparrow$	SSIM $\uparrow$	Parameters
Standard UNet ( $C = 32$ )	39.48	0.956	9.5M
Ours ( $C = 16$ )	40.15	0.957	10.62M
Ours ( $C = 32$ )	<b>40.29</b>	<b>0.962</b>	23.2M

Table 6: Ablation study on the effectiveness of Convolution + Transformer.

better performance with 0.26 dB and 0.004 SSIM promotion, which further justifies the effectiveness of sliding mechanism and the effectiveness of the correspondence between multi-frequency features by incorporating the LF-WSA and HF-SWSA.

**Convolution + Transformer.** We conduct an analysis to verify the effectiveness of Convolutional operator and Transformer. Specifically, we replace all the LF-WSA and HF-SWSA blocks with the ResBlocks [32] and remove the DWT and IDWT operation, resulting in ‘Standard UNet ( $C = 32$ )’ as shown in Table 6. We observe that ‘Ours ( $C = 16$ )’ achieves 40.15 dB and outperforms ‘Standard UNet ( $C = 32$ )’ by 0.67 dB in PSNR and 0.001 in SSIM index with closed parameter number, which verifies that architecture with ‘Convolution + Transformer’ exhibits better local and global context modeling ability than pure CNN-based model. Besides, ‘Ours ( $C = 32$ )’ surpasses ‘Standard UNet ( $C = 32$ )’ by 0.81 dB in PSNR and 0.006 in SSIM with higher parameters, which indicates the effectiveness of ‘Convolution + Transformer’ in real-world denoising. We define  $C$  as the filter number of the convolution layer in each model.

**Effects of Wavelet + Transformer.** To analyze the effectiveness of

Test Set	DND [6]		
Metric	PSNR↑	SSIM↑	Parameters
Standard UNet	39.48	0.956	9.5M
Ours w/o LF-WSA and HF-SWSA	39.97	0.958	22.3M
Ours w/o DWT and IDWT	40.15	0.960	19.5M
<b>Ours Full</b>	<b>40.29</b>	<b>0.962</b>	23.2M

Table 7: Ablation study on the effectiveness of Wavelet + Transformer.

Test Set	DND [6]		
Metric	PSNR↑	SSIM↑	Parameters
$C = 16$	40.15	0.957	10.62M
$C = 32$	<b>40.29</b>	<b>0.962</b>	23.24M
$C = 44$	40.28	0.962	30.56M
$C = 64$	40.18	0.960	48.52M

Table 8: Ablation study on the filter number.

Wavelet + Transformer, we make an ablation study on different network architectures and observe their results on DND benchmark [6]. As shown in Table 7, compared with ‘Standard UNet’, ‘Ours w/o LF-WSA and HF-SWSA’ achieves limited performance improvement with nearly  $2.5\times$  parameter number, which certainly justifies that simply decomposing features using DWT and integrating them using IDWT are useless to real-world image denoising yet bring significant parameter increment. Also, ‘Ours Full’ obviously surpasses ‘Ours w/o DWT and IDWT’ with 0.24 dB and 0.002 SSIM, which justifies the effectiveness of Wavelet + Transformer. Moreover, ‘Ours Full’ exhibits the best results on PSNR and SSIM index benefited from the combination of multi-frequency feature decomposing, integration and building correspondence between them. Therefore, we apply the Wavelet + Transformer architecture in the proposed DnSwin.

**Filter Number.** We make an experiment on the filter number  $C$ . Table 8 shows that ‘ $C = 16$ ’ can achieve a slightly worse performance compared to ‘ $C = 32$ ’ but with lower computation cost. And ‘ $C = 44$ ’ shows a similar performance with ‘ $C = 32$ ’ with obvious parameter increment. However,

Test Set	DND [6]	
Metric	PSNR↑	Parameters
$M = 2$	39.52	8.81M
$M = 4$	39.96	14.52M
$M = 8$	40.29	23.24M
$M = 16$	<b>40.31</b>	40.46M

Table 9: Ablation study on window size.  $M$  is the window size

Test Set	DND [6]	
Metric	PSNR↑	SSIM↑
$\mathcal{L} = \mathcal{L}_1$	40.06	0.958
$\mathcal{L} = \mathcal{L}_{char}$	<b>40.29</b>	<b>0.962</b>

Table 10: Ablation study on loss functions.

when ‘ $C = 64$ ’, the performance will be significantly worse, because a large amount of redundant information introduced by the unnecessary filters may hamper the network performance. Although the performance can be improved with a larger filter number  $C$ , the computational complexity is also increasing, so we choose a compromise filter number  $C = 32$  in order to keep the computational complexity suitable while maintaining better performance.

**Window Size.** We perform an ablation study on the window size  $M$ . Due to the patch boundary artifacts, the patch size (128) should be an integer multiple of the window size. As shown in Table 9, we choose  $M = \{2, 4, 8, 16\}$  to verify the effects of different settings of window size. When ‘ $M = 2$ ’ or ‘ $M = 4$ ’, the window is too small to capture the long-range dependency of pixels, which leads to a significant drop of the model performance. Compared with ‘ $M = 8$ ’, ‘ $M = 16$ ’ only achieves only a marginal performance improvement while significantly increasing the model parameters. Based on the above analysis, we choose  $M = 8$  as the default window size.

**Loss Function.** We compare different setting of loss on the DND Benchmark, is shown in Table 10. ‘ $\mathcal{L} = \mathcal{L}_{char}$ ’ achieves 40.29 dB and the ‘ $\mathcal{L} = \mathcal{L}_1$ ’ obtains 40.06 dB, which justify the effectiveness of  $L_{char}$  loss in real-world image denoising. Moreover,  $L_{char}$  also brings 0.004 gain with SSIM index

Test Set	DND [6]	
Metric	PSNR↑	SSIM↑
$\mathcal{D}_1$ : denoising dataset synthesized by DIV2K	39.42	0.951
$\mathcal{D}_2$ : real denoising dataset SIDD-Medium	39.54	0.952
$\mathcal{D}_1 + \mathcal{D}_2$	<b>40.29</b>	<b>0.962</b>

Table 11: Ablation study on auxiliary training dataset.

compared to  $L_1$ . To this end, we replace  $L_1$  with  $L_{char}$  as default loss function in the model optimization.

**Auxiliary Training Dataset.** We also explore the impact of auxiliary training dataset on model performance. As depicted in Table 11, the results show that using synthesized dataset (i.e., DIV2K  $\mathcal{D}_1$ ) or real-world denoising dataset SIDD-Medium  $\mathcal{D}_2$  lead to lower performance of the model. And that synthetic denoising dataset are more important than real denoising datasets. Since Abdelhamed et al. [15] only collect image pairs in a few indoor scenarios, which makes the trained model overfit these scenarios. However, our model achieves the best score when the model is trained on  $\mathcal{D}_1 + \mathcal{D}_2$ , which verifies that auxiliary training datasets can effectively improve the performance of real-world image denoising.

## 5. Conclusion and future work

In this paper, we propose an effective real-world denoising ViT by incorporating the wavelet sliding-windows mechanism, called DnSwin. We integrate the advantage of the superiority of both CNN and ViT, which not only take the advantage of CNN to process image with large size due to the local receptive field but also take the advantage of self-attention mechanism to capture long-range dependencies. Moreover, with the wavelet feature decomposition, building frequency correspondence between multi-frequency sub-bands and multi-frequency integration, our model can handle different frequency features, especially the noise features of high-frequency and demonstrates a charming result on real-world image denoising. Experimental results on real-world denoising benchmarks demonstrate that our model greatly surpasses the previous state-of-the-art methods with suitable parameter numbers and faster inference time on euclidean-based evaluation protocols.

We aim at extending our work by following directions. First, since the real-world images have more unknown degradation, we would like to change our model to a GAN [58] model so that we can obtain results with better perceptual quality. Second, we are considering extending the DnSwin to handle more general restoration tasks, such as image deblurring, deraining, and super-resolution.

## Acknowledgements

This work was supported in part by the Science and Technology Planning Project of Guangdong Province (no. 2019A050513011), Guangzhou Science and Technology Plan Project (no. 202002030386), National Nature Science Foundation of China (no. U1701266), and Guangdong Provincial Key Laboratory of Intellectual Property and Big Data under Grant (no. 2018B030322016).

## References

- [1] Y. Huang, X. Hou, Y. Dun, J. Qin, L. Liu, X. Qian, L. Shao, Learning deformable and attentive network for image restoration, *Knowledge-Based Systems* 231 (2021) 107384. doi:<https://doi.org/10.1016/j.knosys.2021.107384>.
- [2] Z. Sun, J. Zhao, Z. Zhou, Q. Gao, L1 model-driven recursive multi-scale denoising network for image super-resolution, *Knowledge-Based Systems* 225 (2021) 107115. doi:<https://doi.org/10.1016/j.knosys.2021.107115>.
- [3] C. Bailer, B. Taetz, D. Stricker, Flow fields: Dense correspondence fields for highly accurate large displacement optical flow estimation, in: *Proceedings of the IEEE International Conference on Computer Vision (ICCV)*, 2015, pp. 4015–4023.
- [4] D. Liu, B. Wen, J. Jiao, X. Liu, Z. Wang, T. S. Huang, Connecting image denoising and high-level vision tasks via deep learning, *IEEE Transactions on Image Processing* 29 (2020) 3695–3706.
- [5] M. Singh, M. C. Govil, E. S. Pilli, S. K. Vipparthi, Sod-ced: salient object detection for noisy images using convolution encoder–decoder, *IET Computer Vision* 13 (6) (2019) 578–587.

- [6] T. Plötz, S. Roth, Benchmarking denoising algorithms with real photographs, in: Proceedings of the IEEE/CVF Conference on Computer Vision and Pattern Recognition (CVPR), 2017, pp. 2750–2759. doi:10.1109/CVPR.2017.294.
- [7] M. Lebrun, A. Buades, J. M. Morel, A nonlocal bayesian image denoising algorithm, SIAM Journal on Imaging Sciences 6 (3) (2013) 1665–1688. doi:10.1137/120874989.
- [8] M. Elad, M. Aharon, Image denoising via sparse and redundant representations over learned dictionaries, IEEE Transactions on Image Processing 15 (12) (2006) 3736–3745. doi:10.1109/TIP.2006.881969.
- [9] L. I. Rudin, S. Osher, E. Fatemi, Nonlinear total variation based noise removal algorithms, Physica D: Nonlinear Phenomena 60 (1) (1992) 259–268. doi:https://doi.org/10.1016/0167-2789(92)90242-F.
- [10] S. Guo, Z. Yan, K. Zhang, W. Zuo, L. Zhang, Toward convolutional blind denoising of real photographs, in: Proceedings of the IEEE/CVF Conference on Computer Vision and Pattern Recognition (CVPR), 2019, pp. 1712–1722. doi:10.1109/CVPR.2019.00181.
- [11] Z. Yue, H. Yong, Q. Zhao, D. Meng, L. Zhang, Variational denoising network: Toward blind noise modeling and removal, in: Advances in Neural Information Processing Systems, 2019, pp. 1690–1701.
- [12] C. Tian, Y. Xu, W. Zuo, B. Du, C.-W. Lin, D. Zhang, Designing and training of a dual cnn for image denoising, Knowledge-Based Systems 226 (2021) 106949.
- [13] X. Li, F. Zhou, H. Tan, Joint image fusion and denoising via three-layer decomposition and sparse representation, Knowledge-Based Systems 224 (2021) 107087.
- [14] T. Brooks, B. Mildenhall, T. Xue, J. Chen, D. Sharlet, J. T. Barron, Unprocessing images for learned raw denoising, in: Proceedings of the IEEE/CVF Conference on Computer Vision and Pattern Recognition (CVPR), 2019, pp. 11036–11045.
- [15] A. Abdelhamed, S. Lin, M. S. Brown, A high-quality denoising dataset for smartphone cameras, in: Proceedings of the IEEE/CVF Conference

- on Computer Vision and Pattern Recognition (CVPR), 2018, pp. 1692–1700.
- [16] X. Wu, M. Liu, Y. Cao, D. Ren, W. Zuo, Unpaired learning of deep image denoising, in: Proceedings of the European Conference on Computer Vision (ECCV), 2020, pp. 352–368.
  - [17] T. Huang, S. Li, X. Jia, H. Lu, J. Liu, Neighbor2neighbor: Self-supervised denoising from single noisy images, in: Proceedings of the IEEE/CVF Conference on Computer Vision and Pattern Recognition (CVPR), 2021, pp. 14781–14790.
  - [18] Z. Yue, Q. Zhao, L. Zhang, D. Meng, Dual adversarial network: Toward real-world noise removal and noise generation, in: Proceedings of the European Conference on Computer Vision (ECCV), 2020, pp. 41–58.
  - [19] S. Cheng, Y. Wang, H. Huang, D. Liu, H. Fan, S. Liu, Nbnnet: Noise basis learning for image denoising with subspace projection, in: Proceedings of the IEEE/CVF Conference on Computer Vision and Pattern Recognition (CVPR), 2021, pp. 4896–4906.
  - [20] O. Ronneberger, P. Fischer, T. Brox, U-net: Convolutional networks for biomedical image segmentation, in: International Conference on Medical Image Computing and Computer-Assisted Intervention, 2015, pp. 234–241.
  - [21] F. Yang, H. Yang, J. Fu, H. Lu, B. Guo, Learning texture transformer network for image super-resolution, in: Proceedings of the IEEE/CVF Conference on Computer Vision and Pattern Recognition (CVPR), 2020, pp. 5791–5800.
  - [22] H. Chen, Y. Wang, T. Guo, C. Xu, Y. Deng, Z. Liu, S. Ma, C. Xu, C. Xu, W. Gao, Pre-trained image processing transformer, in: Proceedings of the IEEE/CVF Conference on Computer Vision and Pattern Recognition (CVPR), 2021, pp. 12299–12310.
  - [23] A. Dosovitskiy, L. Beyer, A. Kolesnikov, D. Weissenborn, X. Zhai, T. Unterthiner, M. Dehghani, M. Minderer, G. Heigold, S. Gelly, J. Uszkoreit, N. Houlsby, An image is worth 16x16 words: Transformers for image recognition at scale, in: International Conference on Learning Representations, 2021.

- [24] H. Wu, B. Xiao, N. Codella, M. Liu, X. Dai, L. Yuan, L. Zhang, Cvt: Introducing convolutions to vision transformers, arXiv preprint arXiv:2103.15808 (2021).
- [25] Y. Li, K. Zhang, J. Cao, R. Timofte, L. Van Gool, Localvit: Bringing locality to vision transformers, arXiv preprint arXiv:2104.05707 (2021).
- [26] E. P. Simoncelli, E. H. Adelson, Noise removal via bayesian wavelet coring, in: Proceedings of 3rd IEEE International Conference on Image Processing, 1996, pp. 379–382. doi:10.1109/ICIP.1996.559512.
- [27] A. E. Mahdaoui, A. Ouahabi, M. S. Moulay, Image denoising using a compressive sensing approach based on regularization constraints, Sensors 22 (6) (2022).
- [28] H. C. Burger, C. J. Schuler, S. Harmeling, Image denoising: Can plain neural networks compete with bm3d?, in: Proceedings of the IEEE/CVF Conference on Computer Vision and Pattern Recognition (CVPR), 2012, pp. 2392–2399. doi:10.1109/CVPR.2012.6247952.
- [29] Y. Chen, T. Pock, Trainable nonlinear reaction diffusion: A flexible framework for fast and effective image restoration, IEEE Transactions on Pattern Analysis and Machine Intelligence 39 (6) (2017) 1256–1272. doi:10.1109/TPAMI.2016.2596743.
- [30] K. Zhang, W. Zuo, Y. Chen, D. Meng, L. Zhang, Beyond a gaussian denoiser: Residual learning of deep cnn for image denoising, IEEE Transactions on Image Processing 26 (7) (2017) 3142–3155.
- [31] S. Ioffe, C. Szegedy, Batch normalization: Accelerating deep network training by reducing internal covariate shift, in: International Conference on Machine Learning, 2015, pp. 448–456.
- [32] K. He, X. Zhang, S. Ren, J. Sun, Deep residual learning for image recognition, in: Proceedings of the IEEE/CVF Conference on Computer Vision and Pattern Recognition (CVPR), 2016, pp. 770–778.
- [33] X.-J. Mao, C. Shen, Y.-B. Yang, Image restoration using very deep convolutional encoder-decoder networks with symmetric skip connections, in: Advances in Neural Information Processing Systems, 2016, pp. 2810–2818.

- [34] A. Vaswani, N. Shazeer, N. Parmar, J. Uszkoreit, L. Jones, A. N. Gomez, L. Kaiser, I. Polosukhin, Attention is all you need, in: *Advances in Neural Information Processing Systems*, 2017, pp. 5998–6008.
- [35] Y. Mei, Y. Fan, Y. Zhang, J. Yu, Y. Zhou, D. Liu, Y. Fu, T. S. Huang, H. Shi, Pyramid attention networks for image restoration, *arXiv preprint arXiv:2004.13824* (2020).
- [36] Y. Zhang, K. Li, K. Li, B. Zhong, Y. Fu, Residual non-local attention networks for image restoration, in: *International Conference on Learning Representations*, 2019.
- [37] J. Chen, J. Chen, H. Chao, M. Yang, Image blind denoising with generative adversarial network based noise modeling, in: *Proceedings of the IEEE/CVF Conference on Computer Vision and Pattern Recognition (CVPR)*, 2018, pp. 3155–3164.
- [38] S. Anwar, N. Barnes, Real image denoising with feature attention, in: *Proceedings of the IEEE/CVF International Conference on Computer Vision (ICCV)*, 2019, pp. 3155–3164. doi:10.1109/ICCV.2019.00325.
- [39] D. Kim, J. R. Chung, S. Jung, GRDN: grouped residual dense network for real image denoising and gan-based real-world noise modeling, in: *Proceedings of the IEEE/CVF Conference on Computer Vision and Pattern Recognition Workshops (CVPRW)*, 2019, pp. 2086–2094.
- [40] A. Abdelhamed, R. Timofte, M. S. Brown, Ntire 2019 challenge on real image denoising: Methods and results, in: *Proceedings of the IEEE/CVF Conference on Computer Vision and Pattern Recognition Workshops (CVPRW)*, 2019, pp. 2197–2210.
- [41] N. Parmar, A. Vaswani, J. Uszkoreit, L. Kaiser, N. Shazeer, A. Ku, D. Tran, Image transformer, in: *International Conference on Machine Learning*, 2018, pp. 4055–4064.
- [42] Chen, Jieneng and Lu, Yongyi and Yu, Qihang and Luo, Xiangde and Adeli, Ehsan and Wang, Yan and Lu, Le and Yuille, Alan L., and Zhou, Yuyin, Transunet: Transformers make strong encoders for medical image segmentation, *arXiv preprint arXiv:2102.04306* (2021).

- [43] S. d’Ascoli, H. Touvron, M. Leavitt, A. Morcos, G. Biroli, L. Sagun, Convit: Improving vision transformers with soft convolutional inductive biases, arXiv preprint arXiv:2103.10697 (2021).
- [44] K. Yuan, S. Guo, Z. Liu, A. Zhou, F. Yu, W. Wu, Incorporating convolution designs into visual transformers, arXiv preprint arXiv:2103.11816 (2021).
- [45] Z. Liu, Y. Lin, Y. Cao, H. Hu, Y. Wei, Z. Zhang, S. Lin, B. Guo, Swin transformer: Hierarchical vision transformer using shifted windows, arXiv preprint arXiv:2103.14030 (2021).
- [46] J. L. Ba, J. R. Kiros, G. E. Hinton, Layer normalization (2016).
- [47] G. Elsayed, P. Ramachandran, J. Shlens, S. Kornblith, Revisiting spatial invariance with low-rank local connectivity, in: International Conference on Machine Learning, 2020, pp. 2868–2879.
- [48] A. Vaswani, P. Ramachandran, A. Srinivas, N. Parmar, B. Hechtman, J. Shlens, Scaling local self-attention for parameter efficient visual backbones, in: Proceedings of the IEEE/CVF Conference on Computer Vision and Pattern Recognition (CVPR), 2021, pp. 12894–12904.
- [49] P. Charbonnier, L. Blanc-Feraud, G. Aubert, M. Barlaud, Two deterministic half-quadratic regularization algorithms for computed imaging, in: Proceedings of 1st International Conference on Image Processing, 1994, pp. 168–172. doi:10.1109/ICIP.1994.413553.
- [50] Y. Song, Y. Zhu, X. Du, Grouped multi-scale network for real-world image denoising, IEEE Signal Processing Letters (2020) 2124–2128doi:10.1109/LSP.2020.3039726.
- [51] D. P. Kingma, J. Ba, Adam: A method for stochastic optimization, arXiv preprint arXiv:1412.6980 (2014).
- [52] S. W. Zamir, A. Arora, S. Khan, M. Hayat, F. S. Khan, M.-H. Yang, L. Shao, Learning enriched features for real image restoration and enhancement, in: Proceedings of the European Conference on Computer Vision (ECCV), 2020, pp. 492–511.

- [53] S. W. Zamir, A. Arora, S. Khan, M. Hayat, F. S. Khan, M.-H. Yang, L. Shao, Cycleisp: Real image restoration via improved data synthesis, in: Proceedings of the IEEE/CVF Conference on Computer Vision and Pattern Recognition (CVPR), 2020, pp. 2696–2705.
- [54] S. W. Zamir, A. Arora, S. Khan, M. Hayat, F. S. Khan, M.-H. Yang, L. Shao, Multi-stage progressive image restoration, in: Proceedings of the IEEE/CVF Conference on Computer Vision and Pattern Recognition (CVPR), 2021, pp. 14821–14831.
- [55] Z. Wang, X. Cun, J. Bao, J. Liu, Uformer: A general u-shaped transformer for image restoration, arXiv preprint 2106.03106 (2021).
- [56] J. Liang, J. Cao, G. Sun, K. Zhang, L. Van Gool, R. Timofte, Swinir: Image restoration using swin transformer, in: IEEE International Conference on Computer Vision Workshops, 2021.
- [57] E. Agustsson, R. Timofte, Ntire 2017 challenge on single image super-resolution: Dataset and study, in: Proceedings of the IEEE/CVF Conference on Computer Vision and Pattern Recognition Workshops (CVPRW), 2017, pp. 126–135.
- [58] I. Goodfellow, J. Pouget-Abadie, M. Mirza, B. Xu, D. Warde-Farley, S. Ozair, A. Courville, Y. Bengio, Generative adversarial nets, in: Advances in Neural Information Processing Systems, 2014, pp. 2672–2680.